Prediction of Hysteretic Matric Potential Dynamics Using Artificial Intelligence: Application of Autoencoder Neural Networks

Nedal Aqel[1], Lea Reusser[1,2,3], Stephan Margreth[2], Andrea Carminati[1], and Peter Lehmann[1]*

[1]*Physics of Soils and Terrestrial Ecosystems , ETH Zurich, Switzerland*
[2]*Office for the Environment, canton of Solothurn, Switzerland*
[3]*now at the Swiss Academy of Sciences, Forum Landscape, Alps, Parks (FoLAP), Switzerland*

*Corresponding author, nedal.aqel@usys.ethz.ch, Universitätstrasse 16, 8092 Zurich, Switzerland

Abstract

Information on soil water potential is essential to assess soil moisture state, to prevent soil compaction in weak soils, and to optimize crop management. In lack of direct measurements, the soil water potential values must be deduced from soil water content dynamics that can be monitored at plot scale or obtained at larger scale from remote sensing information. Because the relationship between water content and soil water potential in natural field soils is highly ambiguous, the prediction of soil water potential from water content data is a big challenge. The hysteretic relationship observed in nine soil profiles in the region of Solothurn (Switzerland) is not a simple function of texture or wetting and drainage cycles but depends on seasonal patterns that may be related to soil structural dynamics. Because the physical mechanisms governing seasonal hysteresis are unclear, we developed a deep neural network model that predicts water potential changes using rainfall, potential evapotranspiration, and water content time series as inputs. To adapt the model for multiple locations, we incorporated a Deep Autoencoder Neural Network as a classifier. The autoencoder compresses the water content time series into a site-specific feature that is highly representative of the underlying water content dynamics of each site and quantifies the similarity of dynamic patterns. By adding the Autoencoder's output as an additional input and training the neural network model with three stations located in three major classes founded by the autoencoder, we predict matric potential for other sites. This method has the potential to deduce the dynamics of matric potential from water content data (including satellite data) despite strong seasonal effects that cannot be captured by standard methods.

1. Introduction

The soil water characteristics curve SWC relates the matric potential (MP) and water content (WC) and is the key physical property to quantify soil water dynamics (Tuller and Or, 2023). The SWC (also denoted as soil water retention curve or pressure-saturation relationship) depends on both soil texture and structure and differs with soil types and soil textural classes (Rawls et al., 2003; Shwetha and Varija, 2015). The SWC contains information on the pore size distribution and allows the assessment of flow and transport properties for different hydration states(Menon et al., 2020; Rostami et al., 2015). To provide a complete characterization of the actual soil moisture state and flow regimes, information on both the matric potential and the water content must be specified. Information on volumetric water content is needed to assess the free storage capacity, optimize water management, and to formulate mass balance. The matric water potential is a component of the total and hydraulic soil water potential and determines the water flow in direction of decreasing water potential to achieve equilibrium with its surroundings(Ma et al., 2022). The matric potential is also of particular interest to assess mechanical stability of a soil (Holthusen et al., 2010; Lu et al., 2010). The capillary and adsorptive forces expressed with the matric potential define the unsaturated soil strength mitigating soil compaction by heavy machinery in construction work, farming, and forestry (Smith et al., 2001). For example, matric potential thresholds are defined in various regions of Switzerland to prevent mechanical damage and regulate the maximum load linked to factors like soil type, texture, and vehicle impact (Bundesamt für Energiewirtschaft, 1997). Other important potential thresholds are the wilting point and the field capacity, characterizing the plant available water (Gupta et al., 2023).

It would be optimal to determine the soil moisture status relative to these potential thresholds based on information of water content using the SWC, without direct measurement of the matric potential. In that case, matric potential dynamics could be deduced from remote sensing water content data that are available at various scales. However, the application of this procedure is limited by two effects. Firstly, under saturated conditions, the water potential can change without modifying the volumetric water content. The transition of conditions with negative water potential within the capillary fringe to positive pressures below a water table is crucial for the triggering of landslides (Gallipoli et al., 2003). Secondly,

61 the SWC under field conditions is often an ambiguous relationship between potential and water content

62 due to hysteretic and dynamic effect as will be discussed next.

63 The SWC is typically measured in the lab as series of equilibrium states obtained during drainage, with

64 one water content value assigned to the applied pressure. The results of such small-scale experiments

65 are not sensitive to structural pores that can be found at the field scale (Romero-Ruiz et al., 2018) and

66 can thus be expressed as function of basic soil properties (texture, bulk density, content of organic

67 material) using pedotransfer functions (PTF; Zuo and He, 2021). Because these PTFs ignore the effects

68 of soil structures including macropores and cracks (Basile et al., 2019) and are trained with data from

69 small samples with artificially high initial saturation conditions, their applicability to model dynamic

70 processes in the field is limited. Another limitation is the underlying assumption of an unambiguous

71 relationship between water content and matric potential (and hydraulic conductivity). In all land surface

72 models, water content is linked by an unambiguous relationship between water content and matric

73 potential. In reality, this relationship is highly ambiguous under field conditions as was analyzed in

74 detail by Hannes et al. (2016) and as we will show later in this paper as well.

75 Hannes et al. (2016) analyzed long-term experiments and concluded that the high variation of matric

76 potential values for the same water content are a result of hysteresis, dynamic effects, and structural

77 changes during the season. Hysteresis is related to differences in wetting and drying cycles (Capparelli

78 and Spolverino, 2020) as controlled by different pore structures controlling air- or water invasion and

79 differences in receding or advancing wetting angles (Fomin et al., 2023). Hysteresis is often manifested

80 in coarse textured soils and occurs as well during slow processes. Another process resulting in an

81 ambiguous pressure-saturation relationship is dynamic effects with water contents that are not in

82 equilibrium with the quickly changing potential (Ross and Smettem, 2000). Finally, the size of

83 structural pores is not constant with time but changes with season, water content, and soil formation

84 processes (Fu et al., 2021). The combined effect of hysteresis, non-equilibrium, and structural changes

85 makes it extremely challenging to deduce soil matric potential from information on water content. Also,

86 the implementation of these combined effects in physically-based models of unsaturated water flow is

87 not straightforward. As an alternative approach to physically-based models, machine learning can be

88 applied to simulate the complex relationship between matric potential and water content under field
89 conditions. In this study, we will apply a deep neural network (DNN).

90 Deep neural networks (DNN) have demonstrated their effectiveness as a powerful numerical tool for
91 resolving complex patterns. Their ability to learn from data and recognize intricate relationships makes
92 them valuable in various fields, including the modeling of soil water characteristics. For example, Jain
93 et al. (2004) and Achieng (2019) used artificial neural network (ANN) models to predict the hysteretic
94 water content from observed matric potential values. However, both publications simulated lab data
95 under equilibrium conditions and cannot be applied for the more complex dynamic processes in the
96 field. In addition, the models were site-specific and needed both water content and matric potential
97 information for the training. Here we will apply a different DNN using an autoencoder approach. As
98 we will explain in the theory section, the autoencoder condenses the complexity of temporal (and
99 spatial) patterns into a single (or a few) number(s). The hypothesis of this study is that the autoencoder
100 value is a new and unique characterization of the soil moisture dynamics and can be used to predict
101 matric potential dynamics from observed water content data. The paper is organized as follows: in
102 section 2, the study sites and the basics of the deep neural network with the autoencoder approach are
103 presented. The results section compares the model performance of site-specific deep neural network
104 (DNN) and shows the possibility to build a generalized DNN using the autoencoder analysis as model
105 input. Limits and possible applications of the model approach are discussed in section 5.

2. Material and methods

107 In a first step, matric potential time series were simulated at nine sites in the region of Solothurn
108 (Switzerland) using site specific ANN model, to proof that the ANN models can predict matric potential
109 from water content dynamics with site specific training. In the next step, the autoencoder analysis of
110 water content dynamics of all sites was conducted. Finally, the site-specific ANN model was enhanced
111 and transformed into a multisite model by combining two deep neural networks. This transformation
112 allowed for a more comprehensive and versatile predictive framework of matric potential as function
113 of water content.

2.1 Study area and soil moisture data

The study area covers mainly the canton of Solothurn in Switzerland (Fig.1), and thus an area of approximately 629 km^2. The climate in Solothurn is classified as oceanic climate (Cfb) according to Koppen and Geiger climate classification, with an average yearly temperature of 9.5 °C and annual precipitation of around 1400 mm. Approximately half of the annual precipitation in the canton undergoes the process of evaporation (Spreafi and Weingartner, 2005). During the year, the average temperature varies by 19 °C with the highest temperature occurring in the month of July and the lowest average temperature in January. Regarding precipitation patterns, the month of June has the highest level of precipitation, while March stands out as the driest month. Soil moisture dynamics (see below) were studied for the period from 2011 to 2022. For this period, climatic data was available on the data portal of MeteoSwiss (IDAWEB, 2024) . The data was gathered from the closest meteorological stations to each of the nine sites in the Solothurn region.

Soil moisture data were downloaded from the 'soil monitoring network' (BODENMESSNETZ, 2024) collecting data from 65 stations distributed over eleven cantons of Switzerland. The network's primary objective is to provide real-time soil moisture information for mitigating soil compaction. BODENMESSNETZ also plays a role in raising awareness among farmers and foresters about soil compaction, providing a tool to assess the current situation and adjust the use of heavy machinery based on weather conditions. As the network has been running since 2011, it now serves as a valuable resource by offering long-term diverse information, including land use, precipitation amounts, and matric potential measured at various depths (20 and 35 cm depth in most of the stations, using T8 and T32 tensiometers from METER group). Only at nine sites that are located in the region of Solothurn, the water content was measured at 20 cm depth (Stevens Hydra Probe). For these nine sites, daily values in volumetric water content (20 cm), matric potential (20 cm) and precipitation values were used. The matric potential in the downloaded data was given in kPa and was transferred to matric potential head with units of cm (1 cm is 0.1 kPa), considering a water density of 1000 kg m^{-3} and gravity acceleration of 10 m s^{-2}.

140 As the soil moisture decreases, water is drawn from the tensiometer, creating a negative pressure or

141 tension. During dry periods, cavitation may occur, causing water vaporization and air bubble formation

142 (Mendes and Buzzi, 2013), or tensiometers had to be refilled (Sadeghi et al., 2018). To address these

143 challenges and ensure accurate data collection, various data preprocessing and filtering techniques were

144 implemented. These techniques involved identifying and removing outliers, systematically excluding

145 data points with water potential values within the problematic dry ranges and filtering out data points

146 with extremely low or high water content values. The study also flagged abrupt changes in volumetric

147 water content (VWC) and matric potential (MP) for further investigation, as these could indicate

148 measurement anomalies. Additionally, a thorough analysis of weekly trends in the data was conducted

149 to identify systematic variations over time (see Appendix A).
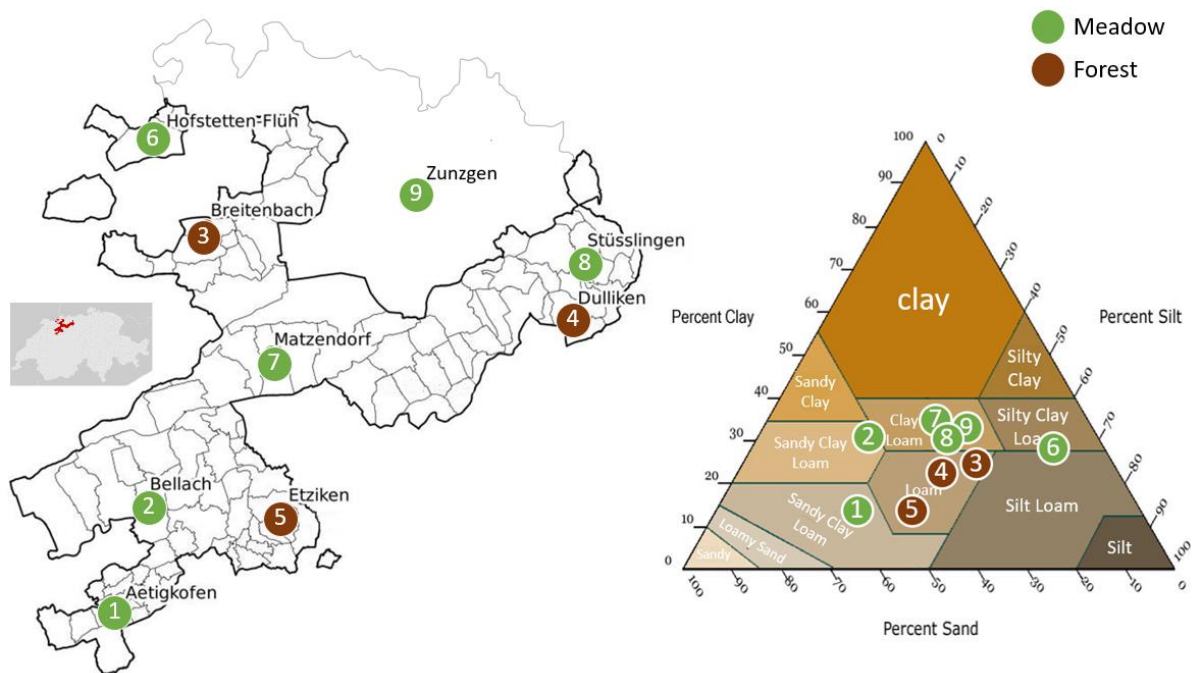
150

151 **Figure 1** Overview of the study area with site locations, soil texture, and land cover. The primary focus
152 is on the canton of Solothurn, outlined by the black border on the map, with an additional site from the
153 canton of Basel (site 9, Zunzgen). Within this region, three sites are categorized as forests, while the
154 remaining six sites are designated as meadows. The analyzed soil horizons (20 cm depth) of the study
155 area encompasses five soil textural classes as shown in the soil texture triangle.

156 The analyzed soil horizons of the selected locations can be assigned to five different soil textural classes

157 (figure 1) and two different land covers (meadow and forest). The location denoted as Matzendorf (site

158 #7) contains the highest clay content, whereas locations such as Aetigkofen (site #1) are predominantly

159 sandy. Across these nine locations, different relationships between matric potential and water content

160   were deduced from field data as shown in Figure 2 for two sites with low and high variations in water

161   content for similar potential values. To show the relevance of seasonal patterns, we differentiate

162   between summer (April to September) and winter period (remaining months).

163

164
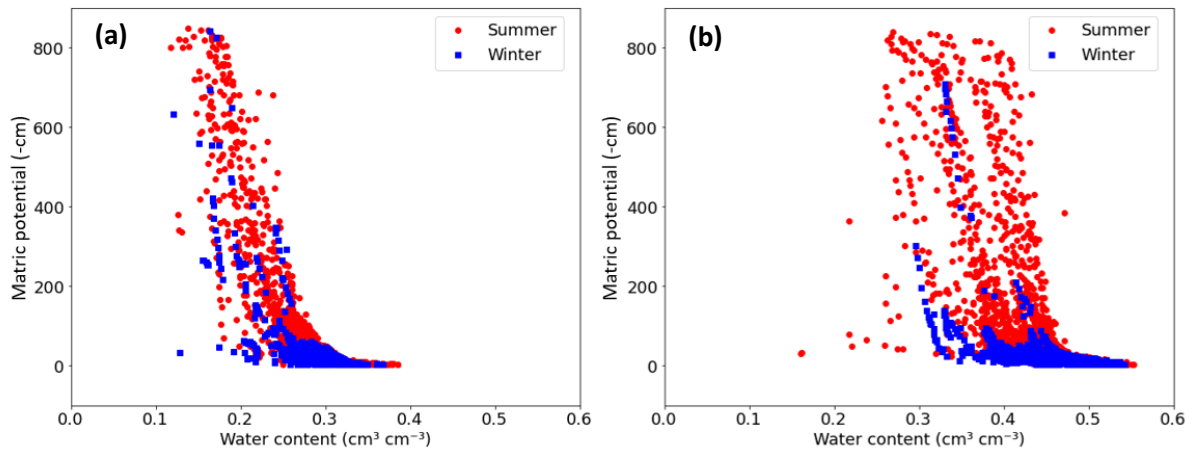
Figure 2 Soil-Water characteristics curve (SWC) measured in the field at two sites classified into
summer (April to September) and winter period (remaining months) from 2012 to 2023. **(a)** The Etziken
site (site #5) shows small changes in the SWC dynamics over the years, for both the warm and cold
period. **(b)** A contrasting scenario was found for the site in Bellach (site #2) that was characterized by
a wide range of water content for similar potential values. The unit of matric potential, represented as -
cm, is equivalent to -0.1 kPa.

2.2 Deep neural network (DNN)

A basic artificial neural network (ANN) comprises one or two hidden interconnected layers, with each

layer tasked with the conversion of an input vector ($\boldsymbol{x}$) into a hidden state vector ($\boldsymbol{h}$), as described by

(Bertels and Willems, 2023). This conversion is accomplished with eq. (1):

$$\boldsymbol{h} = f(\boldsymbol{x}) = act(\mathbf{W} \bullet \boldsymbol{x} + \boldsymbol{b}) \tag{1}$$

Where $f(\boldsymbol{x})$ represents the transformation function applied to the input vector($\boldsymbol{x}$), with a weight matrix

($\mathbf{W}$) and a bias vector ($\boldsymbol{b}$), integrated with an activation function (denoted as "act").

To construct a deep neural network (DNN), multiple layers (more than two hidden layers) are

interconnected to form a 'multilayer perceptron.' The training process involves finding optimal values

for the weights and biases in the network using suitable optimization techniques (Bertels and Willems,

2023). In this study, DNN was built to predict the daily MP for the nine sites. The process involved

several key steps. First, in the design of the neural network, activation functions were carefully selected

183 and integrated to introduce non-linearity into the model's transformations (Montesinos López et al.,

184 2022). The Rectified Linear Unit (ReLU) activation function was employed to mitigate vanishing

185 gradient problem and enhance the model's ability to handle noisy input. The inclusion of ReLU was

186 motivated by considerations of computational efficiency, with some attention given to the potential

187 issue of "dying ReLU" (Lu, 2020; Montesinos López et al., 2022).

188 Next, the neural network was structured with a total of six layers, including four hidden layers as

189 suggested by Achieng (2019). All layers were densely connected, fostering strong information flow

190 between neurons. Crucially, batch normalization was incorporated after the second hidden layer. Batch

191 normalization is a technique that normalizes the activations within a layer during training, which can

192 help mitigate issues like internal covariate shift and accelerate convergence (Ioffe and Szegedy, 2015).

193 The choice of the optimization method was the Adam optimizer, a powerful tool for training neural

194 networks. It adaptively adjusted learning rates, thereby optimizing the learning process, and enabling

195 rapid convergence while employing Mean Squared Error (MSE) as the loss function (Kingma and Ba,

196 2014). To prevent overfitting by the Adam optimizer, an early stopping mechanism was implemented.

197 This mechanism continuously monitored the loss function for the hold out data during training, ceasing

198 the process if no improvement or a sudden increase was detected over a predetermined number of

199 consecutive epochs.

200 The initial deep neural networks (DNN) were configured with 4 input parameters and the daily

201 logarithmic scaled matric potential (MP) value as output. The input parameters consisted of

202 precipitation, potential evapotranspiration, measured VWC, and the weekly percentage change in

203 VWC. As the prediction process progressed, two major issues were identified. Firstly, the influence of

204 the VWC measurements on the training process was found to be predominant. Consequently, a decision

205 was made to increase the weight of precipitation and potential evapotranspiration in the calculation

206 process by incorporating three new input parameters: the weekly total precipitation and

207 evapotranspiration (the sum of the current day and the preceding six days), along with the difference

208 between these two new components. Secondly, the use of logarithmic scaled MP values was found to

209 be highly sensitive to data availability. Therefore, a decision was made to retrain the model using

210   absolute linear MP values (see Appendix B). In total, the final model was equipped with 7 input

211   parameters to predict the absolute linear MP values for a given location. For each site, a site-specific

212   DNN was built. The extent of the training data is predominantly influenced by site-specific

213   characteristics. For instance, sites characterized by sandy soils necessitated a shorter training duration

214   in contrast to sites with a higher clay content. Typically, the training dataset spanned a duration of 4 to

215   7 years. During this period, 70% of the data were randomly selected for training, while the remaining

216   30% were set aside as holdout data (Gholamy et al., 2018). The extra years of data beyond the initial

217   training period were reserved for validation purposes.

218   2.3 Autoencoder neural network

219   The autoencoder, consisting of an encoder and a decoder, is an unsupervised deep neural network that

220   learns how to efficiently compress input data into a meaningful representation and subsequently

221   reconstruct the original data from this compressed form (Chen and Guo, 2023). By connecting the

222   encoder and decoder, the autoencoder effectively captures important patterns and variations present in

223   the data, enabling comprehensive analysis and interpretation (Chen and Guo, 2023). In this study, an

224   autoencoder neural network (figure 3) was built to analyze the measured VWC time series at 20 cm

225   depth for the 9 sites.
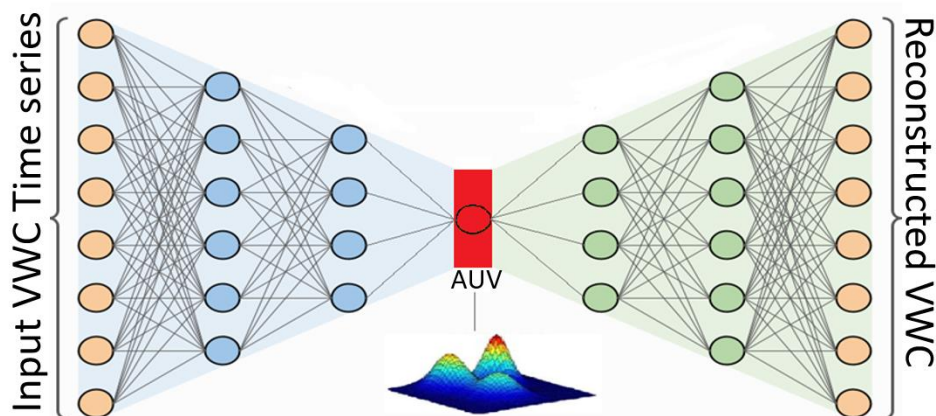
226

227   **Figure 3** Autoencoder deep neural network for volumetric water content dynamic analysis. In this
228   illustration, a densely connected autoencoder is utilized to compress the dynamic information of
229   Volumetric Water Content (VWC) into a singular value, AUV, highlighted in red. The process begins
230   with the encoder, depicted in blue, extracting the AUV from the measured volumetric water content
231   time series (left orange layer). Subsequently, the densely connected decoder, represented in green,
232   utilizes the AUV to reconstruct the VWC (orange layer at the right). Both the encoder and decoder,
233   characterized by dense connections, optimized the AUV value by minimizing the error between the
234   measured VWC and the reconstructed VWC.

235   The process was as follows. Firstly, an encoder neural network was created for each site. Its objective

236   was to take the VWC time series as input and gradually reduce its dimensionality through hidden layers

237   (Chen and Guo, 2023). The encoders' output was a single site-specific latent representation, called

238   Autoencoder Value (AUV), and captures essential features of the VWC dynamics (Chen and Guo,

239   2023). Subsequently, a decoder neural network was developed to utilize the AUV value as reference to

240   reconstruct the original VWC time series data. The success of this reconstruction depends on the

241   training process, which aimed to optimize the AUV value by minimizing the error between the original

242   VWC time series and its reconstructed counterpart by minimizing the mean squared error (MSE) value

243   to less than 0.1.

244   After the optimization process, for each site one autoencoder value (AUV) was obtained. These AUV

245   were scaled and then used to build a combined model (Figure 4) as follows. The AUV were sorted into

246   three categories. Subsequently, one site from each category was selected. Finally, the data from the

247   three chosen sites, each representing one category, were used to train the combined AUC-DNN model.

248   The final combined model was thus equipped with 8 input parameters to predict the dynamic MP for a

249   specific location. These parameters consisted of the same 7 inputs employed in the DNN model (section

250   2.2), complemented by the AUV. The neural network structure, as detailed in section 2.2, remained

251   unchanged, employing the same optimization techniques.
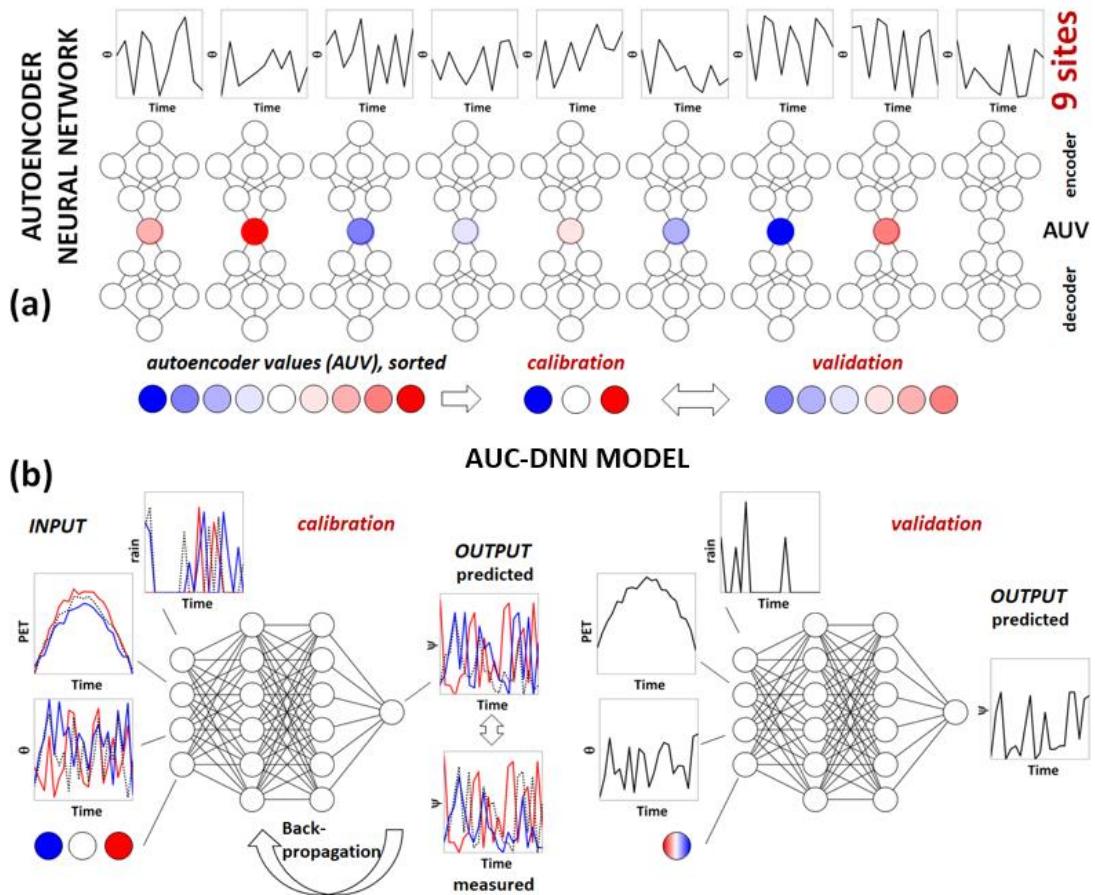
Figure 4 Application of two different types of deep neural network for the prediction of matric potential ψ. In this conceptual example, the water moisture dynamics of nine sites is considered. **(a)** The autoencoder neural network captures the characteristic features of the soil water content (θ) dynamics, assigning an autoencoder value (AUV) to each site. These values are sorted to AUV classes (one site from each class was used for calibration, remaining sites for validation). **(b)** The combined AUC-DNN model is built using the calibration sites with rainfall, potential evapotranspiration (PET), water content, and AUV as part of the 8-input parameters. The predicted matric potential (ψ) is compared to measured values for backpropagation. The calibrated DNN is then used to predict ψ for the remaining sites.

Initially, 70% of the data from each of the training sites were randomly selected for the training dataset. Subsequently, the remaining 30% of the data were set aside as the holdout dataset, serving as a benchmark for assessing model performance. The developed AUC-DNN was then applied for the other six sites (with the same input variables including AUV) to predict the entire datasets of those unseen sites. The combined model has thus the strengths of both components—the DNN' ability to understand dynamic MP patterns and the feature extraction capabilities of the autoencoder. This shift in the model's strength extends it from being site-specific to encompassing multiple sites, enabling it to gain a broader understanding of how the dynamic MP and AUV values relate.

2.4 Statistical evaluation

The evaluation of model performance is carried out by comparing the model predictions to the measured data. While there is no universal consensus on a standardized evaluation procedure, it is widely recognized that a multi-objective approach should be adopted e.g., (Boyle et al., 2000; Willems, 2009). In this study, a combination of four evaluations tools was adopted. First, a scatter plot of observations against simulated values was utilized to visualize the degree of alignment with the identity line (often referred to as the 1:1 line). This graphical approach allowed for a qualitative assessment of model performance. A closer concentration of data points near the 1:1 line indicated higher agreement between calculated and observed values. Moreover, this graphical method includes the 95 % confidence interval area which help in scrutinizing the model's consistency across different prediction ranges and detecting potential biases within the model's performance (Ritter and Muñoz-Carpena, 2013).The second criterion evaluates the distribution of (signed) prediction errors (eq(2)). Ideally, the error distribution should be centered around zero, following a normal distribution pattern around this point with low standard deviation. Such a distribution indicates an unbiased model with errors that tend to balance out. Deviations from this pattern may suggest model bias or other unexpected characteristics in the prediction errors PE (den Ouden et al., 2012).

$$PE = O_i - P_i \tag{2}$$

with observed O_i and predicted matric potential value P_i. The third evaluation metric was the root means squared error (RMSE; eq (3a)). RMSE with a value of zero indicates perfect fit, while higher RMSE value means worse model performance (Ritter and Muñoz-Carpena, 2013). The final criterion for model evaluation involved the use of the dimensionless goodness-of-fit indicator (eq (3b)), known as the coefficient of efficiency (NSE; Nash and Sutcliffe, 1970). NSE, which ranges from negative infinity to 1, serves as an indicator of model performance, with a value of 1 indicating a perfect fit, while a negative NSE suggests that using the means of the observed values is a better representative for the data than the evaluated model itself (Gupta and Kling, 2011; Ritter and Muñoz-Carpena, 2013). A NSE value > 0.75 indicates a very good model, while an NSE value < 0.5 signifies unsatisfactory results (Moriasi et al.,

295 2007). In Gupta et al. (1999) a threshold NSE-value of 0.80 was used for good model performance and

296 is applied here as well. The RMSE and NSE are defined by:

297 $$RMSE = \sqrt{\frac{\sum(O_i - P_i)^2}{N}}$$ (3a)

298 $$NSE = 1 - \frac{\sum(O_i - P_i)^2}{\sum(O_i - \bar{o})^2}$$ (3b)

299 where O_i represents the measured value, P_i the simulation output, and $\bar{o}$ the mean of the observed values,

300 all within the context of a sample size N.

3. Results

302 Following the model discussion in section 2.2 and 2.3, we present first the results of the site-specific

303 tests of predicting matric potential dynamics with a deep neural network (water content, rainfall and

304 evapotranspiration as input data), before the role of autoencoder value is considered.

3.1 Deep neural network modeling without autoencoder

306 The site-specific DNN model was used to simulate the time series for all nine sites. In Figure 5, the

307 results are shown for the Stüsslingen site (size #8, clay loam, meadow). The model was trained on data

308 that had 1825 days of observations from January 2012 to January 2020. The data was split randomly

309 into two parts: 1) a calibration dataset that had 1277 days and 2) a holdout dataset that had 548 days.

310 The model was then validated on data from February 2018 to January 2023 (1379 days). A strong

311 agreement between the model and the observed data was discovered in both the training and validation

312 datasets (figure 5c) as reflected by the low RMSE value and the high NSE value (table 1). Furthermore,

313 it was noticed that the error distribution exhibited a predominantly normal pattern with minimal bias

314 towards higher observed values compared to the predicted values (figure 5d). These findings suggest

315 that the site-specific DNN-model was not only able to be generalized well to unseen data but also

316 demonstrated a reliable ability to predict MP.

317 The statistical evaluation (Table 1) reveals a consistent performance across both the training and

318 validation periods for the Stüsslingen site, offering compelling evidence that the model avoids

319 overfitting. Additionally, when it comes to predicting MP values, the 95 % confidence interval indicates

320 that the model can capture well the overall dynamics (Figure 5b). However, the model performance

321 exhibits higher deviations for values exceeding 400 cm and consistently underestimates values higher

322 than 600 cm (figure 5b), which could explain the mild positive skewness observed in the distribution

323 of prediction errors in figure 5d.

324
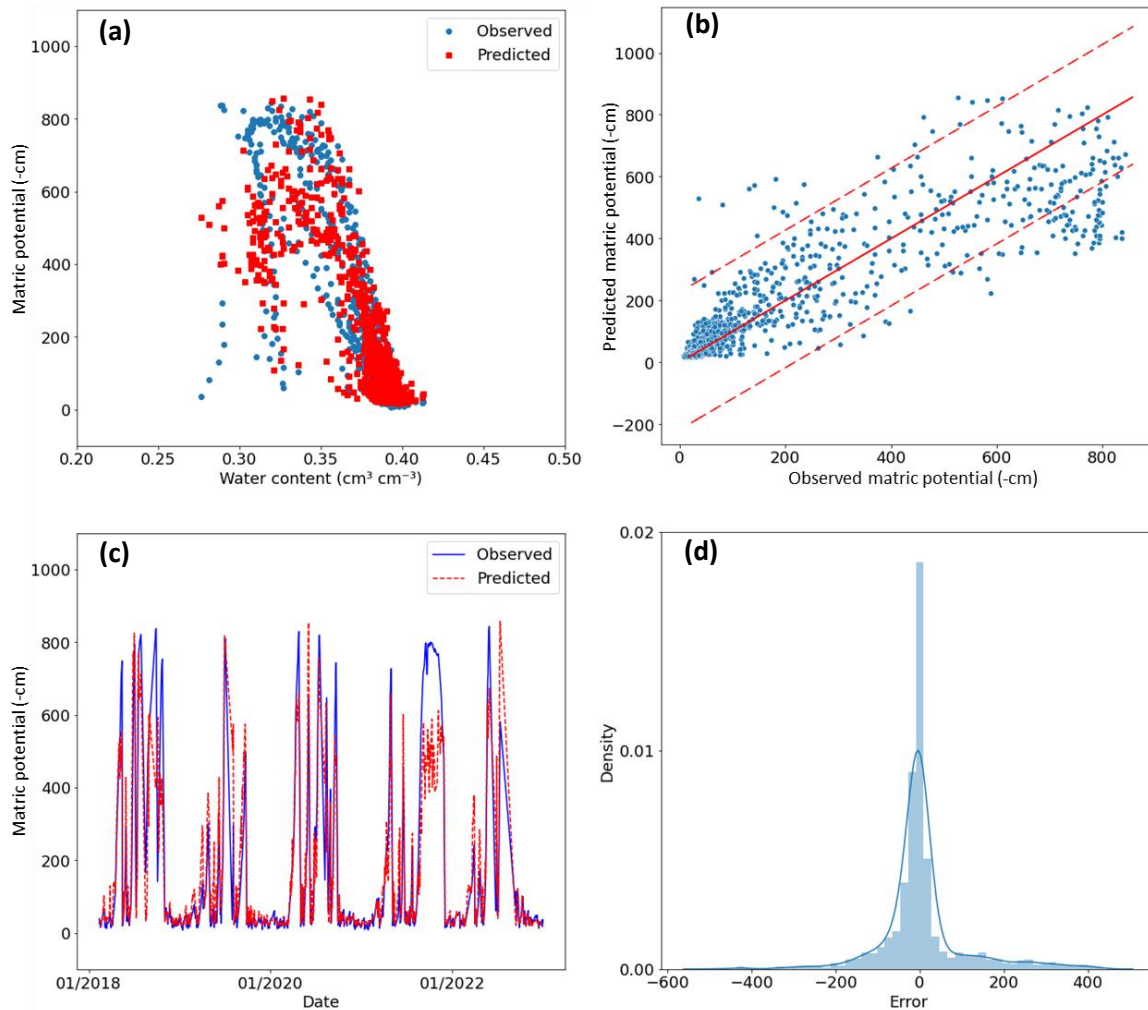
Figure 5 Graphical evaluation of the performance of the site-specific deep neural network (DNN) for validation for the Stüsslingen site (site #8) for the validation period 2018 to 2022. **(a)** Comparison between the simulated and measured soil water characteristics curve. **(b)** Scatter plot comparing simulated and measured matric potential values, providing a visual representation of the level of conformity to the identity line. The two dashed lines represent the 95% confidence interval around the identity line, providing a visual assessment of the level of agreement. **(c)** Model validation presenting time series with the observed and predicted matric potential. **(d)** Analysis of the distribution of prediction errors (observed minus predicted values) with positively mild skewed distribution

333 Comparing the performance for the 'holdout' period (randomly chosen days between 2012 and 2019)

334 of the nine site-specific DNN models, the NSE index is larger than 0.55 ('good') for all and larger than

335 0.80 ('optimal') for six sites. For all sites it was thus possible to build a DNN model with good model

performance for the randomly chosen test days. However, for the validation period, only four showed

optimal performance (NSE > 0.80). For two forest sites with an optimal performance for the holdout

period (Dulliken, site #4, and Etziken, site #5), the NSE dropped from a range between 0.82 and 0.88

to a range between 0.73 and 0.75 (table 1). Obviously, the model captured the overall short term

dynamics during training (randomly chosen days) but faced problems in the precise prediction of the

long validation period. An extended training period may be necessary to enhance the model's accuracy

for these specific sites. Three grassland sites (Bellach, site #2, Matzendorf, #6, and Hofstetten-Flüh, #5)

showed good but not optimal performance already during the holdout period. As discussed in the next

section, this may be related to large variations of the pressure values for similar water contents and the

corresponding large AUV. Notably, the lower performance observed in the holdout period for

Hofstetten-Flüh could be also linked to data limitations, as only 1200 days were used to train the model

for this specific site (compared to 1825 sites for the other sites).

Table 1 Statistical assessment of calibration (1825 days, until year 2019/2020) and validation results
(years 2018/2019/2020 until years 2020/2021/2022) for nine sites. The holdout dataset was part of the
training period and includes 548 days (30 % of calibration).

Location	AUV (-)	Training (holdout)		Validation	
		NSE (-)	RMSE (-cm)	NSE (-)	RMSE (-cm)
1 Aetigkofen	1.95	0.92	48	0.89	60
2 Bellach	7.00	0.70	98	0.62	125
3 Breitenbach[a, b]	3.56	0.86	82	0.83	96
4 Dulliken[a]	2.19	0.82	55	0.73	103
5 Etziken[a]	1.90	0.88	56	0.75	70
6 Hofstetten-Flüh[b]	5.59	0.76	90	0.63	123
7 Matzendorf	6.39	0.76	83	0.59	133
8 Stüsslingen	4.49	0.80	71	0.80	98
9 Zunzgen	6.44	0.87	62	0.83	73

[a] forest sites.
[b] Sites with limited available data. For those sites, only 1200 days were used for training; Within this training period, a subset
of 360 randomly selected days was designated as a holdout dataset; the validation period for those specific sites was from
2018/2019 to 2022.

3.2 Autoencoder DNN

The Autoencoder values (AUV) deduced from the time series analysis of the volumetric water content

for the period 2012-2022 can be classified in three main groups (figure 6). Soil water characteristics

curves (SWC) with low water content at saturated conditions and a small variation of water content for

359 similar potential values are assigned to 'type 1', contrasting 'type 2' with large water content values

360 and variations. These types of SWC are related to small ('type 1') and high ('type 2') autoencoder

361 values (AUV). Sites with AUV between these two classes, are denoted in the following as 'transitional'

362 type. As shown in Table 1, the AUV of forest soils are small (mainly 'type 1') with large NSE values.

363 In contrast to the forest soils, there are grassland sites with high AUV ('type 2') but small NSE.

364 Probably, the high variations of the SWC curve for 'type 2' require longer training periods to capture

365 the high variations in the pressure-saturation relationship.
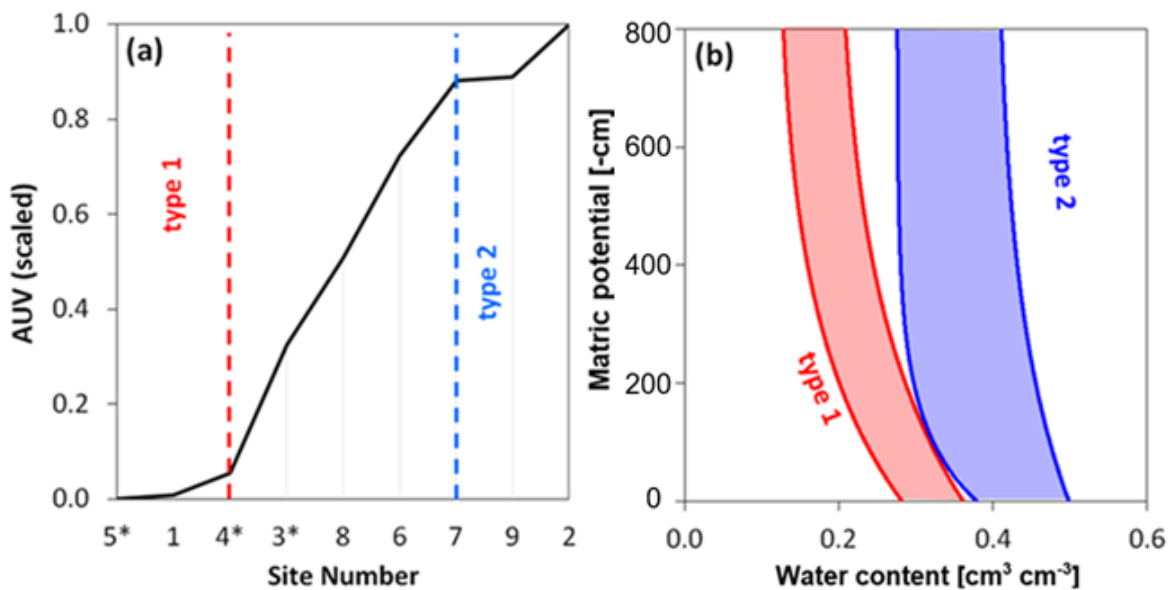
366

367 **Figure 6** Autoencoder value (AUV) and its relation to the soil water characteristics curve (SWC). **(a)**
368 The AUV of the nine sites with three sites of small (type 1) and three sites of high (type 2) AUV. **(b)**
369 The type 1 of the SWC has small water contents close to saturation and a narrower range of water
370 contents for similar water contents compared to type 2 with high water content values and variations.
371 Type 1 shows the data range of Aetigkofen (site #1) and Type 2 for Bellach site (#2). The site numbers
372 are chosen in alphabetic order and as shown in Figure 1 (Aetigkofen (1), Bellach (2), Breitenbach (3),
373 Dulliken (4), Etziken (5), Hofstetten-Flüh (6), Matzendorf (7), Stüsslingen (8), Zunzgen (9); sites with
374 forest are marked with *).

375 ### 3.3 Deep neural network using the autoencoder value (AUC-DNN)

376 As mentioned in the previous section, the nine sites could be grouped into three main types according

377 to the scaled autoencoder value (AUV). Consequently, it was assumed that the creation of a DNN

378 model, which incorporates AUV in conjunction with the previously built site-specific neural network,

379 could enable predictions for unseen sites. Ideally, the model should be trained with a balanced dataset,

380 including one site from the 'type 1' category, one site from the 'type 2' category, and a few sites from

381 the 'transitional' category to capture the full transition between the 'type 1' and 'type 2'. However, due

to the data limitation, the model was trained for only three sites representing the three types (Etziken, site #5, for 'type 1'; Bellach, #2, for 'type 2'; Stüsslingen, #8, for the 'transitional type') and was then used to predict the six unseen sites. The impact of the small training set (only one site for transitional type) was clear in the model results, which exhibited some instability, changing from one run to another as the model was not able to assume the same transitional function between sites consistently. Therefore, the model was run 20 times, then the average result for theses runs was taken as a representative outcome. The application of the new DNN model with AUV to predict the dynamic of matric potential is shown in Figure 7 for Breitenbach (site #3, loam, forest) as unseen site. The model was found to fell slightly behind the previously designed DNN model, but still can predict the dynamic in a good way. Notably, the NSE value for this model for Breitenbach site was 0.71 over the entire period from 2012 to 2022 (Table 2).

Table 2 AUC-DNN Model performance for the period 2012-2022. Three training sites were used to build the AUC-DNN model that was then applied for the other six sites. The sites are listed according to the corresponding autoencoder value (AUV). The asterisks mark the sites with forest; The AUV was scaled from 1.9 to 7.0 to simplify input. Alternatively, scaled values ranging from 0 to 1 could also be utilized.

Location	AUV	AUV (type)	used as	NSE (-)	RMSE
5 Etziken*	1.90	Type 1	Training site	0.82	70
1 Aetigkofen	1.95	Type 1	Validating site	0.76	88
4 Dulliken*	2.19	Type 1	Validating site	0.65	100
3 Breitenbach*	3.56	Transitional	Validating site	0.71	73
8 Stüsslingen	4.49	Transitional	Training site	0.85	116
6 Hofstetten-Flüh	5.59	Transitional	Validating site	0.60	113
7 Matzendorf	6.39	Type 2	Validating site	0.58	123
9 Zunzgen	6.44	Type 2	Validating site	0.69	104
2 Bellach	7.00	Type 2	Training site	0.71	104

It was noticed that the error distribution exhibited a predominantly normal pattern with a bias towards higher observed values compared to the predicted values (figure 7d). The analysis indicates the model's proficiency in forecasting dynamic trends rather than precise values (figure 7c). The results align with the anticipated scenario as the AUV for Breitenbach (3.56) was relatively close the Stüsslingen AUV value (4.49). Therefore, the underestimation detected in Stüsslingen for the site-specific DNN (figure 5b) is expected to exist in Breitenbach as well. The average model performance for all sites is presented

405 in Table 2. The NSE values was > 0.55 for the 6 unseen sites (validating sites) and provided strong

406 evidence that the model can be relied upon for the dynamic MP predictions.

407
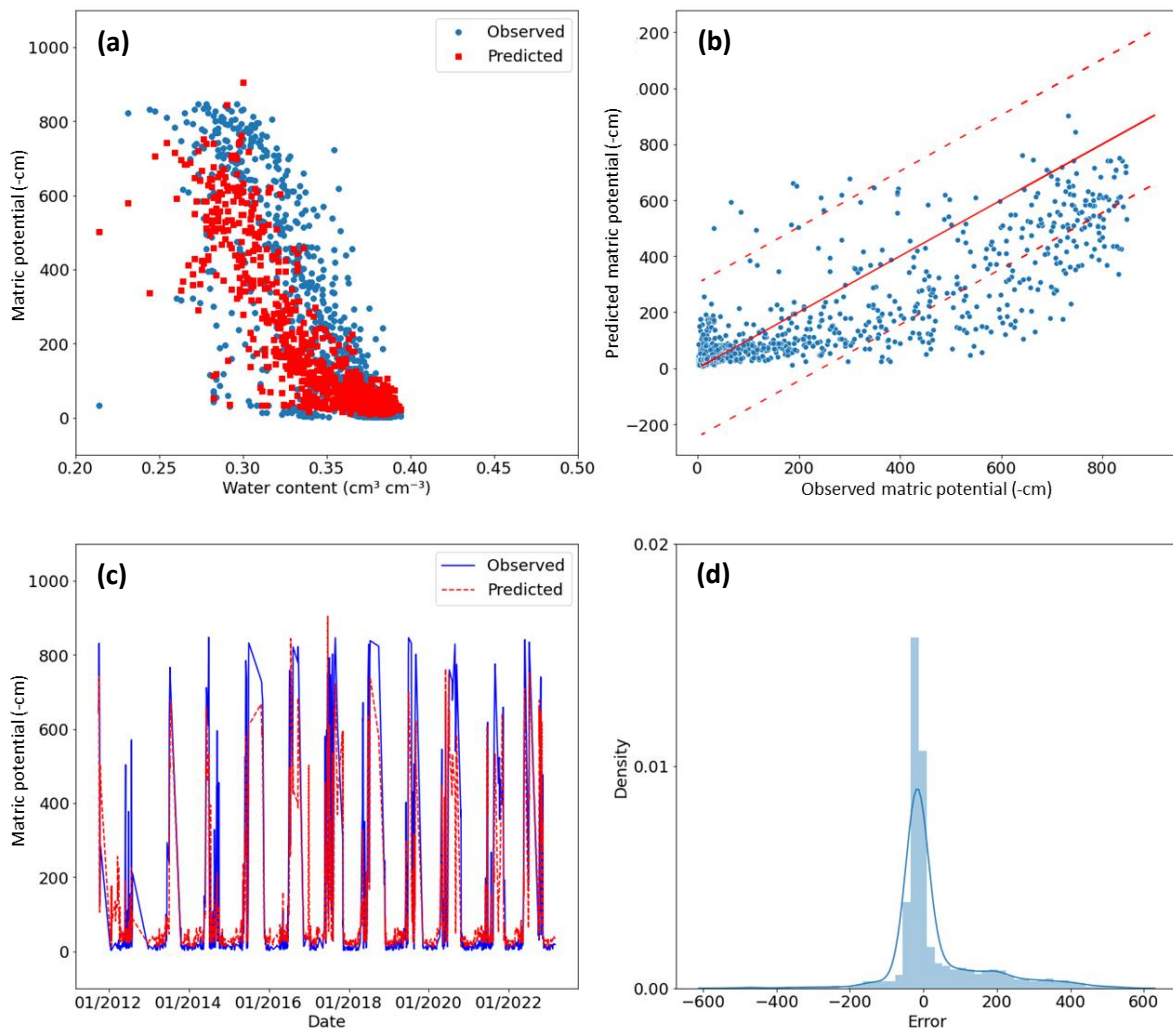
Figure 7 Evaluation of the Deep Neural Network with Autoencoder (AUC-DNN) model performance at the Breitenbach site for the period 2012-2022. **(a)** Comparison between the expected Soil Water characteristics curve (SWC) and the observed SWC. **(b)** Scatter plot that compares observed data points with their corresponding simulated values, providing a visual representation of the level of conformity to the identity line. The two dashed lines represent the 95% confidence interval around the identity line, providing a visual assessment of the level of agreement. **(c)** Time series comparison showing the observed and predicted matric potential for the entire period. **(d)** Analysis of the distribution of prediction errors (observed minus modelled value) using positively mild skewed distribution.

416 The NSE values for the unseen sites (validating sites) varied from 0.58 to 0.76, indicating a spectrum

417 of model performance, ranging from acceptable to good. The low NSE values observed for Matzendorf

418 (site #7) suggest that the model's utility is more suited for capturing overall trends and dynamics rather

419 than precise values. This evaluation was further supported by examining a scatter plot (Figure 8) that

420 compares the observed data points with their corresponding simulated values for the sites scored the

421 lowest and the highest NSE, Matzendorf (site #7) and Aetigkofen (site #1). The plot revealed a wider

422 95% confidence interval for Matzendorf (figure 8a) in comparison to Aetigkofen (figure 8b), indicating

423 that the lower the NSE value is, the more challenging it became for the model to predict the exact MP

424 values. However, the model performance indicated the ability of the AUC-DNN model to predict

425 dynamic MP without the necessity of site-specific training data, marking a transition from the DNN

426 site-specific nature to a more versatile multi-site model.
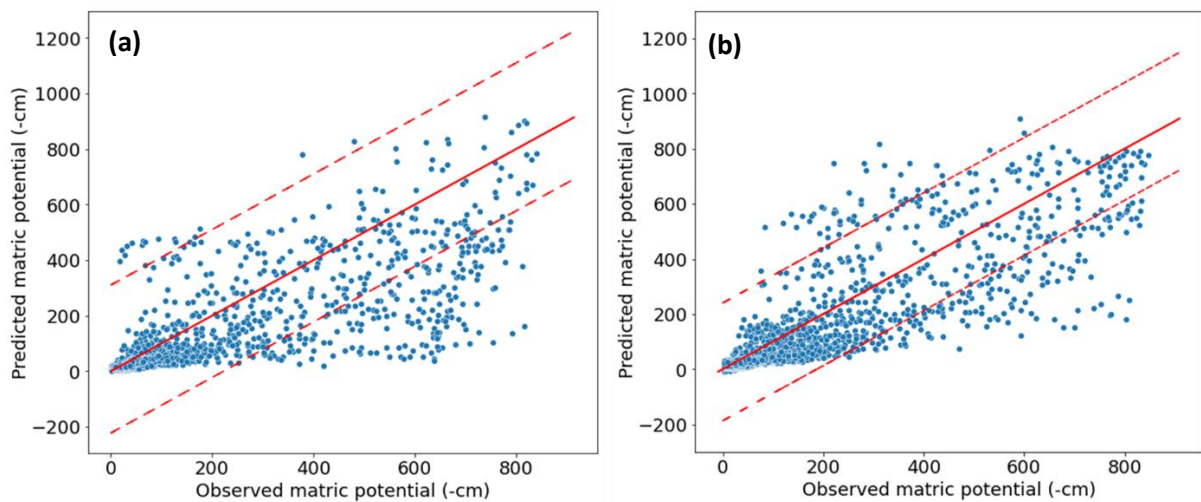
427

428 **Figure 8** Comparison between observed data points and their corresponding simulated values for two
429 sites with lowest and highest efficiency coefficient NSE. **(a)** Matzendorf (site #7) with NSE of 0.58. **(b)**
430 Aetigkofen (site #1) with NSE of 0.76. The solid lines mark the 1:1 correspondence, the dashed lines
431 the 95% confidence interval.

4. Discussion

433 Based on the analysis of the simulation results presented in section three, it can be asserted that the

434 model was successfully built. However, as discussed in the next subsection, the model is expected to

435 have certain drawbacks due to the limited number of available sites. In the other subsections, the

436 relationship between the autoencoder value and soil properties and its application for satellite data will

437 be discussed.

4.1 Limits of the deep neural network with autoencoder value (AUC-CNN)

439 First, the model's statistical evaluation revealed that the matric potential (MP) at a depth of 20 cm could

440 be simulated with acceptable precision. However, a high variability in the evaluation is indicated by the

441 NSE values for the unseen sites. This variance is attributed to the model's limited generalization

442 capacity, as it was trained on just three sites. Furthermore, the model was not able to catch the whole

443 dynamic for the training sites due to the limited length of available data. For example, Bellach (site #2),

444 a training site that has a high AUV, had NSE value of 0.71 for the training period (table 2), which

445 indicates that the model was able to catch the general trend for this site, but still can't predict the exact

446 value of the MP. The effect of this result was obvious on the sites that are closed to AUV 'type two'

447 category (e.g., Hofstetten-Flüh and Matzendorf, sites #6 and #7, with NSE of 0.60 and 0.58,

448 respectively).

449 The stability of the AUC-DNN model was insufficient, as the model showed different prediction quality

450 upon running the model repeatedly for the same training sites (figure 9). This variability in the outcomes

451 indicates that the model can find different MP dynamics scenarios inside the training data. Therefore,

452 it is recommended to train the model for more than one site in the same AUV type.
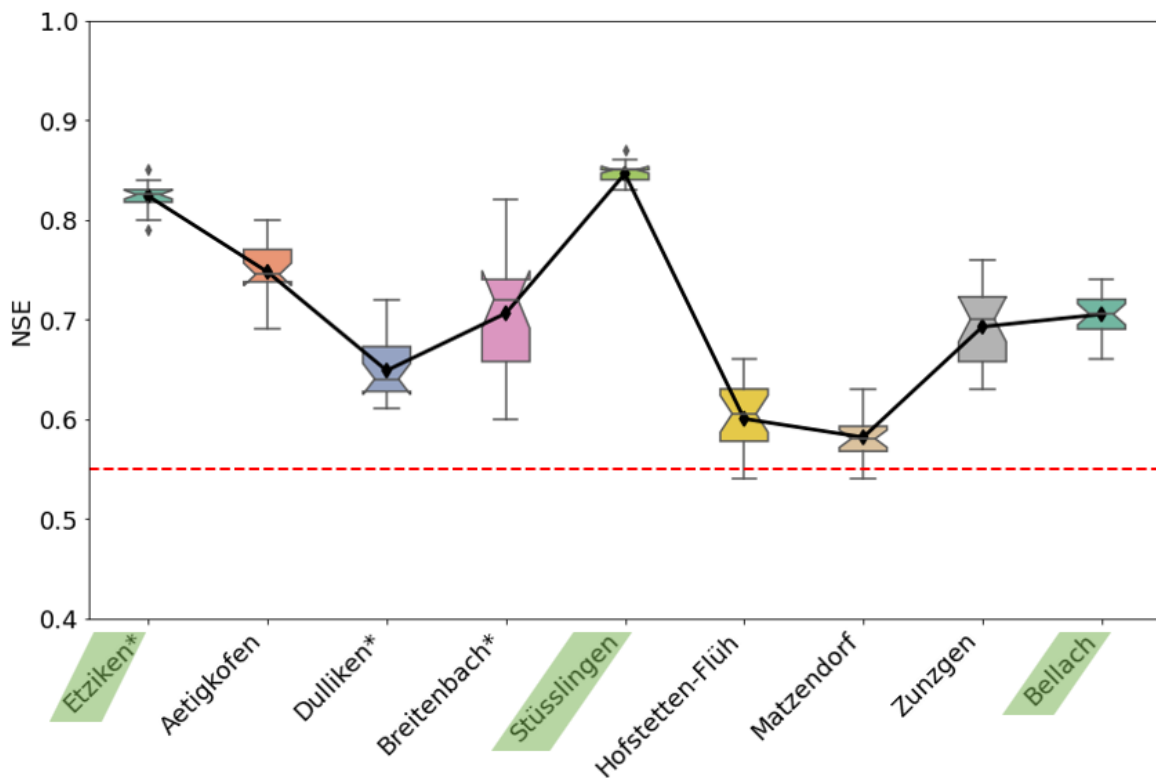
453

454 **Figure 9** Variation of prediction results for 20 Runs for the AUC-DNN model quantified with the
455 efficiency coefficient NSE. The highest variation was with the unseen sites in the transitional and type
456 2 categories. Each box represents the interquartile range, with the line inside denoting the median. The
457 black diamond markers connect the mean values for each station, providing insight into the central
458 tendency of the data. Notches on the boxplots offer a visual indication of the uncertainty around the
459 median. The red dashed line represents the defined threshold for the NSE, set at 0.55 ; sites with forest
460 are marked with *; training sites are highlighted in green.

461   Especially for the 'transitional type', choosing a site in the beginning, in between, and in the end of the

462   category would stabilize the modeling results. However, in this study, there was no possibility to

463   provide the model with extra data to solve the prediction instability. Therefore, a solution was

464   implemented by 1) closely monitoring the model manually to ensure it captures the dynamic from all

465   three sites. This involved training the model with nearly identical time periods for each site and visually

466   confirming comprehensive coverage of the cloud of points for the retention curve of each site, avoiding

467   concentration on specific patterns during training. The process also includes 2) running the model for

468   20 times, then averaging the results. Additionally, the statistical evaluation plots as shown in Figure 8,

469   were used to detect instances with very low or very high MP prediction values.

470   For the set of sites analysed in this study, the model showed good generalization capacity and stability.

471   However, the nine sites were similar with respect to climate and geology and the range of soil textural

472   classes (see Figure 1) was relatively narrow. In a future study, the AUC approach will be applied for

473   sites differing in climate and soil textural classes. We expect that the model can predict the dynamic

474   matric potential for a new site as long as the autoencoder value falls within the range of AUV of the

475   training sites. To predict the soil moisture dynamics for soils with autoencoder values outside of the

476   range of training data, the model must be re-built using additional training data.

477

478   4.2 Interpretation of AUV and its relationship to physical soil properties

479   As discussed in section 3.2, the autoencoder value (AUV) is low for soil water characteristics curves

480   (SWC) with low saturated water content and low variations of water content for a certain matric

481   potential value (type 1) and high AUV for large values and variations of water content (type 2). To

482   provide a more quantitative relationship between SWC and AUV, the SWC data were characterized as

483   follows: the time average of volumetric water content (VWC) and SWP were calculated for 15 days for

484   the period 2015 to 2022. The envelope of these data was then calculated by fitting a minimum and

485   maximum pressure saturation relationship including the averaged data (see Figure 10a).
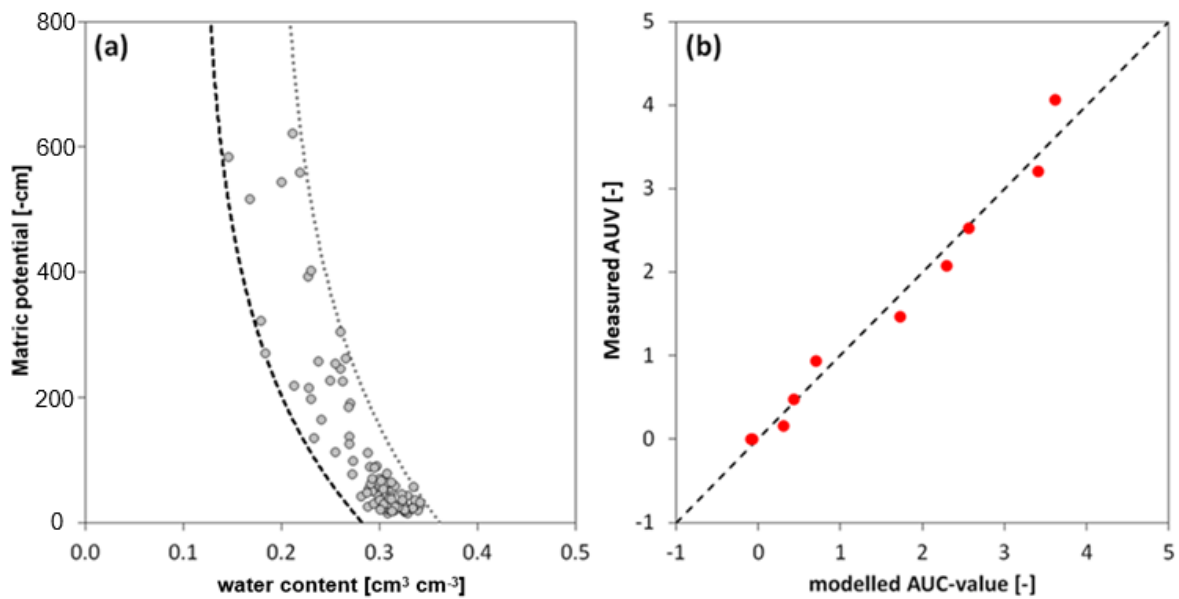
486

487   **Figure 10** Relationship between autoencoder value (AUV) and soil water characteristics curve (SWC).
488   **(a)** 15-days average of SWC data for Aetigkofen (symbols; site #1). The two lines are exponential
489   functions building the envelope of the SWC curve. **(b)** Linear model for the nine sites linking the
490   parameters of the exponential model with the 'measured' AUV (deduced from measured water content
491   data).

492   The two boundary lines of the SWC were then characterized by a 'saturated' and 'residual' water

493   content and a shape parameter defining an exponential decrease of water content with increasing

494   absolute matric potential values. The SWC of each site can thus be described by six parameters (three

495   parameters per boundary line). As shown in Figure 10b, a linear model expressing the AUV as function

496   of these six parameters can be built. Simpler models with less parameters could not reproduce the AUV

497   of all sites. Despite the positive correlation between AUV and average water content, the average water

498   content alone is not sufficient to explain the range of AUV for all sites. Also combining average water

499   content with soil texture information could not reproduce the AUVs of all sites, indicating that the soil

500   moisture dynamics represented by AUV is not only dependent on static soil textural attributes but

501   seasonal structural features as well.

502   Accordingly, there is no simple interpretation of AUV based on texture and average water content, but

503   the dynamic variation of water content must be considered as well. Due to the relevance of the variation

504   in water content for similar matric potential value, the use of a variational autoencoder (VAE) instead

505   of the typical autoencoder could be considered. In contrast to the typical autoencoder that maps the

input information into a single point (or a few points), the VAE produces a probability distribution

capturing the variability (second moment) of the data. This could be specifically of interest for clay

soils with high water contents (much larger than the residual water content) for the entire range of matric

potential values. By including a probabilistic approach in the compressing and decompressing step, the

variability of the data could be captured more efficiently using VAR.

4.3 Application for satellite data

The AUC-DNN model was used to analyze satellite-based volumetric water content (VWC) satellite

data, including SMAP L4 and L3, SMOS products, and Sentinel data. Subsequently, a comparison was

carried out for the AUV for both site-specific measurements and earth observation (EO) measurements

for the same region. The initial findings highlighted a disparity between the dynamics captured by EO

products and the actual dynamics. Therefore, if the objective is to establish a robust system capable of

detecting changes in water retention dynamics on a regional scale, it is considered necessary to enhance

the calibration of EO in Europe. Only with EO-data that can reproduce the essential of the soil moisture

dynamics as manifested in the AUV, the matric potential dynamics can be deduced from EO-data. For

future EO-data with improved capacity to capture regional soil moisture dynamics, the concept

presented in this study (AUC-DNN) could be used to predict matric potential dynamics at global scale

(see Appendix C).

5. Summary and conclusions

The soil water potential (SWP) determines water flow direction, water ability for plants, and mechanical

stability. Because it cannot be measured directly by remote sensing techniques at larger scales, it is

often deduced from water content information, assuming an unambiguous relationship between water

content and SWP. However, this relationship under dynamic field conditions is highly ambiguous due

to hysteresis, dynamic effects, and soil structural changes that cannot be modeled with a physically-

based model. To enable prediction of SWP from soil water content, we apply a deep neural network

(DNN) with an autoencoder to define unique features of the soil moisture dynamics. By inserting the

532   autoencoder value (AUV) together with climatic data and water content measured at nine sites in the

533   region of Solothurn (Switzerland) in a deep neural network (AUC-DNN), the soil water potential could

534   be predicted. The main findings of the study can be summarized as follows:

535   • The SWC of the nine sites can be classified in three types based on the width of pressure-
536   saturation relationship and the water content close to saturation

537   • These SWC-types are manifested in different autoencoder values (AUV)

538   • The AUV is not a simple function of average water content or soil texture but includes structural
539   effects as well

540   • The AUC-DNN model could predict successfully the SWP dynamics of sites without site-
541   specific training

542   The autoencoder value (AUV) is thus a new descriptor of the complex soil moisture dynamics that

543   cannot be captured with physically based models. Future satellite generation may be sensitive enough

544   to measure the AUV from remote sensing water content data. The approach presented in this paper will

545   then enable the prediction of the soil matric potential at the global scale using remote sensing water

546   content data.

547   Appendix A: Data Quality Assurance and Trend Analysis

548   As a precaution for data quality, the Absolute Matric Potential (AMP) and volumetric water content

549   (VWC) data were scrutinized to identify potential errors the data. The process includes different steps

550   that were necessary to discover anomalies, checking the integrity of the data, and detecting systematic

551   changes with time.

552   **1- Flagging Abrupt Changes in VWC and MP:**
553
554   **VWC Flagging and removing:**

555   • Differences between consecutive (daily) time steps in the water content time series were
556   calculated.

- Instances with daily differences exceeding 0.1 cm^3/cm^3 were flagged and denoted as sudden decreases or increases in VWC.

- Instances with VWC below 0.1 cm^3/cm^3 or exceeding 0.7 cm^3/cm^3 were identified and removed from the dataset. These extreme values were considered as measurement anomalies or outliers affecting the overall dataset's reliability.

- Instances with AMP<1 cm was removed from the data to overcome limitations in the used method. The water potential can change without modifying the volumetric water content after this limit, which could make the results of the model not accurate enough.

- The differences between consecutive time steps in AMP -time series was calculated; instances with daily differences exceeding 500 cm were flagged and called sudden decreases or increases in AMP (figure A1).

- The threshold AMP-value of 850 cm was employed in a specific step, where instances with AMP exceeding 850 cm were removed from the dataset, addressing the physical properties of water as it starts to boil in the tensiometers under pressure after this limit.

- Periods of concurrent decrease in AMP (indicator for wetting) and decrease in VWC (drying) were flagged (figure A1).

- Periods with matric potential values remaining constant over a three-day rolling window were flagged (figure A1).

2- Utilizing Index Windows for Data Manipulation and Data Removal

To address flagged instances mentioned before, a systematic approach is employed. For each flagged instance, three additional indices are generated around it to construct an index window, spanning one day before (index_1), the flagged instance itself (index_0), and two days after (index_2 and index_3). This four-day index window was eliminated from the dataset (figure A1). The decision to eliminate this window was informed by a visual assessment of measurements as it was noticed that when a measurement error occurs, the accuracy of the preceding day is affected. Furthermore, it was assumed that the device requires two subsequent

583   days to restore normal measurement precision. This process contributes to a refined dataset,

584   providing a more accurate representation of the underlying trends in AMP and VWC.
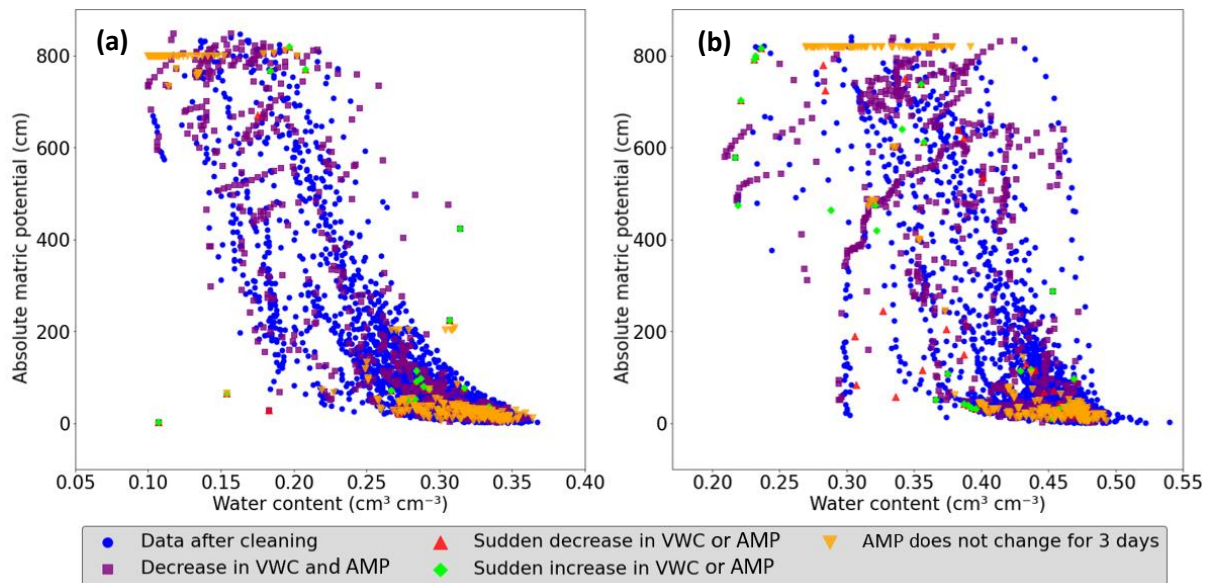
585

586   **Figure A1** Comparison of data before and after cleaning procedure: the blue circles depict the remaining
587   data after applying the cleaning criteria. Each distinct marker represents eliminated points, each
588   corresponding to a specific criterion (e.g., the square purple marker for simultaneous decrease in
589   volumetric water content (VWC) and the absolute matric potential (AMP), the red upward-pointing
590   triangle is the marker for sudden decreases, the lime diamond for sudden increases, and the orange
591   downward-pointing triangle marks periods of unchanged AMP). This provides insights into the reasons
592   for data removal and illustrates the profound impact of the data cleaning process in retaining high-
593   quality data points. In **(a)** the cleaning process for sandy clay loam site in Aetigkofen (site #1) is shown,
594   in **(b)** the cleaning process for the Matzendorf site (site #9, clay loam soil).

Appendix B: Running the model with Logarithmic MP value.

595

596   The AUC-DNN showed a good performance in predicting the dynamic MP for the different 6 unseen

597   sites. However, it was clear that the model prioritizes tends to focus on capturing significant changes in

598   values rather than accurately representing the values themselves. This tendency is attributed to the

599   substantial difference between the highest and lowest absolute values (approximately 850 cm), leading

600   the model to emphasize major fluctuations while neglecting minor ones. To address this issue and

601   enhance the model's precision in capturing the exact AMP, a suggestion has been made to train the

602   model for the same three sites but with the logarithmic value for the AMP. This modification aims to

603   strike a better balance, ensuring that both major and minor changes are effectively captured while

604   maintaining accuracy in representing the specific values of MP.

605 To qualitatively assess the model training performance under the logarithmic scale, a scatter plot (Figure

606 B1) was generated, comparing observations against simulated values for the second training site

607 (Stüsslingen). The reason for choosing a training site was to understand how the model captures the

608 dynamics when trained with logarithmic matric potential. The results suggest that using logarithmic

609 scale, the model prioritized the prediction of the exact absolute value of matric potential (AMP), which

610 makes the model to optimize predictions for the absolute values between 0 to 200 cm. This approach is

611 giving the same importance to small and large changes in the AMP, which causes that the model

612 assigned a higher weight to small changes according to their higher frequency, while neglecting less

613 frequently occurring major dynamic shifts. Consequently, the model's accuracy went down beyond 200

614 cm (figure B1a) when compared to the model trained on non-logarithmic AMP-values (figure B1b). To

615 maintain a balanced consideration of changes, logarithmic MP was avoided in the main part of the

616 paper.

617
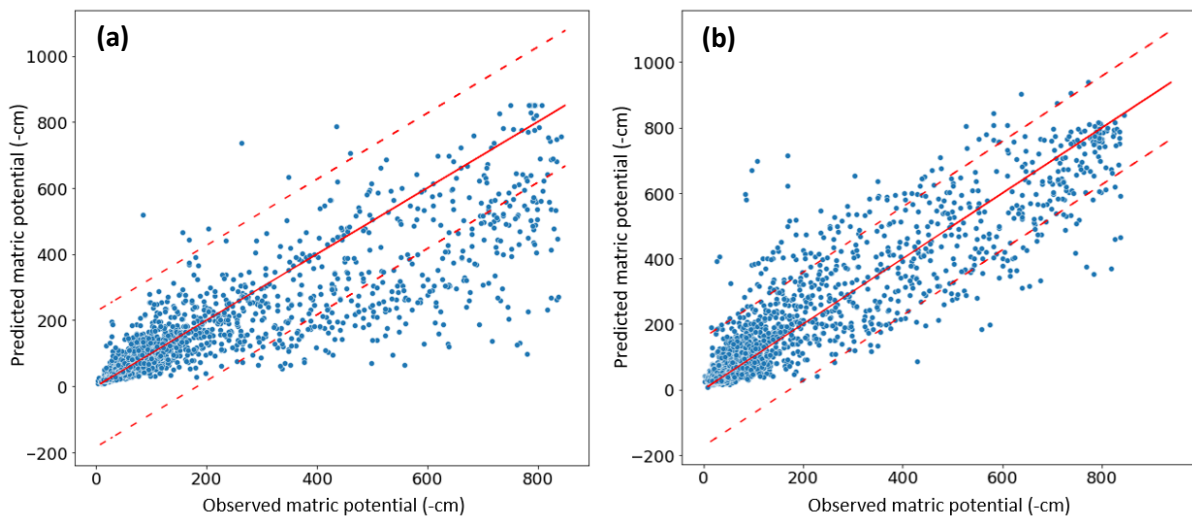
618
619 **Figure B1** Visual comparison of model performance, comparing the observed and simulated values for
620 the Stüsslingen training site. **(a)** the model trained with logarithmically scaled AMP-values, while in
621 **(b)** The model trained with absolute linear matric potential (AMP) values. The solid line denotes the
622 1:1 correspondence, and dashed lines represent the 95% confidence interval.

623 ## Appendix C: SMAP data and Autoencoder for global scale analysis

624 SMAP (Soil Moisture Active Passive) is a NASA satellite mission that was established to help in

625 improving weather forecasts and global drought monitoring. SMAP data products are available at

626 different levels of processing, from Level 1 (L1; instrument measurements) to Level 4 (L4; model-

derived value-added products). For this study, SMAP L3 and SMAP L4 products for measuring moisture content were used. The main difference between the two products is that SMAP L3 depends on the passive radiometer measurements, while SMAP L4 products are derived from a data assimilation system that combines the L-band brightness temperature observations from SMAP with a land surface model and meteorological forcing data (Reichle et al., 2019). SMAP L3 products for moisture content are primarily affected by vegetation and surface roughness, allowing them to capture surface soil moisture variations. In contrast, the incorporation of land surface models in SMAP L4 products reduces its sensitivity to vegetation covers and surface roughness, making the products more representative of the profile soil moisture conditions (Reichle et al., 2019).

The autoencoder's encoded representations offer a unique opportunity to compare the spatial patterns inherent in "point measurement" with remote sensing data such as SMAP L3 and SMAP L4 data. The autoencoder method could illuminate how these diverse data streams align or diverge, providing crucial insights into the compatibility and complementarity of ground and satellite measurements. The process was applied for the data between the years 2015 to 2022. All the data (SMAP L4, SMAP L3, and on-site measurements) were given to the autoencoder neural network together. Subsequently, the resulting autoencoder values were scaled. Finally, a comparison was made to show if the satellite measurements and the on-site measurements have the same measured dynamics.

The autoencoder analysis of SMAP L3 (figure C1) indicates that satellite measurements struggle to capture the dynamic change of the water content, as all locations yield approximately the same Autoencoder Value (AUV). In contrast, the SMAP L4 product (figure C1) exhibits fluctuations in AUV results. For instance, Stüsslingen and Matzendorf align closely with on-site measurements in terms of AUVs. However, for Hofstetten-Flüh, the SMAP L4 product indicates a very small AUV, suggesting an expected dynamic in line with a type 1 soil water retention curve (figure 6b). In contrast, on-site measurements indicate a higher AUV for Hofstetten-Flüh, suggesting a closer association with a type 2 soil water retention curve. These findings underscore the imperative for developing a new methodology to calibrate satellite data in the Switzerland area. The prevalent uniformity in SMAP L3 results and the notable disparities between on-site measurements and satellite data across various

654 products highlight the need for a more refined approach to ensure accurate and reliable dynamic soil

655 moisture assessments.

656
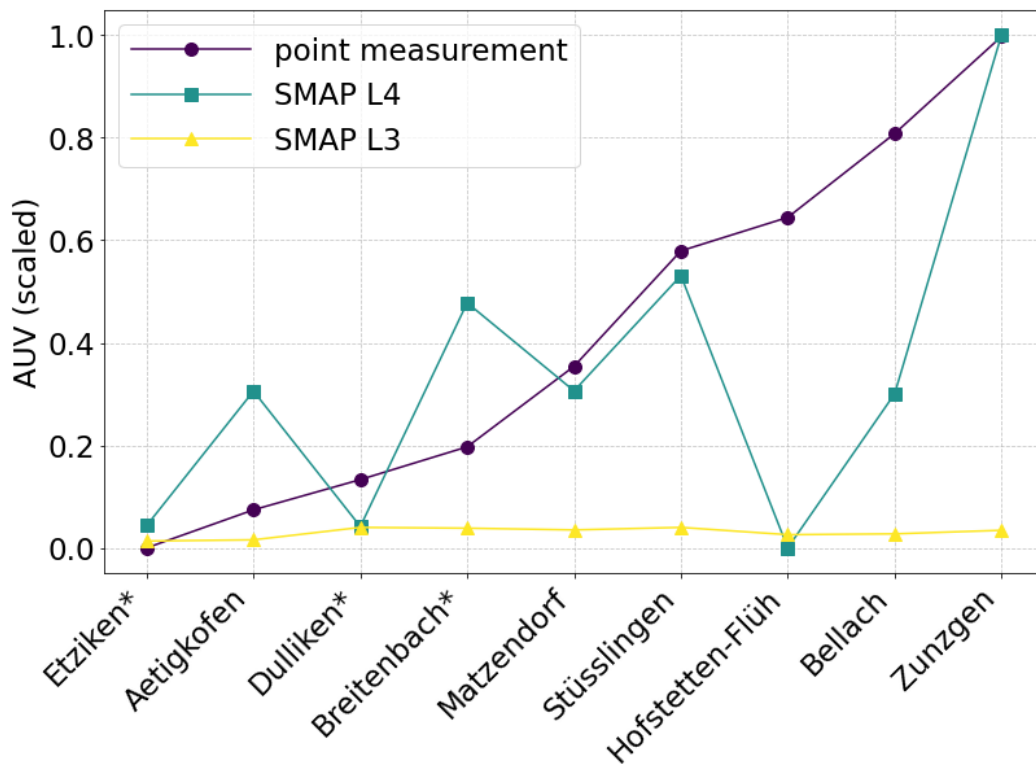
Figure C1 Comparative analysis of Autoencoder Neural Network results for SMAP L3 and SMAP L4
satellite data, alongside with profile measurements. The fluctuating AUV values indicate varying
degrees of alignment with on-site measurements across different locations. Sites with forest are marked
with *.

Code and data availability

662 The related input data for the AUC-DNN model and Python code are openly accessible under

663 https://doi.org/10.5281/zenodo.10600669 and https://doi.org/10.5281/zenodo.10602397 respectively.

664 The input for the autoencoder and its python codes are openly accessible under

665 https://www.doi.org/10.5281/zenodo.10605108

Author contributions

667 NA, AC, and PL designed the research. NA and PL performed the research. NA and MR analyzed the

668 soil moisture time series. SM was responsible for the soil moisture network. NA wrote the codes and

669 built the model. NA and PL wrote the manuscript with substantial input from all co-authors.

Competing interests

The contact author has declared that none of the authors has any competing interests.

Financial support

"This research is part of the project Artificial Intelligence for Soil Health. Funded by the European Union. Views and opinions expressed are however those of the author(s) only and do not necessarily reflect those of the European Union or of the Research Executive Agency (REA). Neither the European Union nor the granting authority can be held responsible for them."

Acknowledgements

NA acknowledges the utilization of ChatGPT to enhance coherence within certain sections of the manuscript.

References

Achieng, K. O.: Modelling of soil moisture retention curve using machine learning techniques: Artificial and deep neural networks vs support vector regression models, Comput Geosci, 133, 104320, https://doi.org/10.1016/j.cageo.2019.104320, 2019.

Basile, A., Bonfante, A., Coppola, A., De Mascellis, R., Falanga Bolognesi, S., Terribile, F., and Manna, P.: How does PTF Interpret Soil Heterogeneity? A Stochastic Approach Applied to a Case Study on Maize in Northern Italy, Water (Basel), 11, 275, https://doi.org/10.3390/w11020275, 2019.

Bertels, D. and Willems, P.: Physics-informed machine learning method for modelling transport of a conservative pollutant in surface water systems, J Hydrol (Amst), 619, 129354, https://doi.org/10.1016/j.jhydrol.2023.129354, 2023.

BODENMESSNETZ: https://www.bodenmessnetz.ch/messwerte/datenabfrage, last access: 22 July 2024.

Boyle, D. P., Gupta, H. V., and Sorooshian, S.: Toward improved calibration of hydrologic models: Combining the strengths of manual and automatic methods, Water Resour Res, 36, 3663–3674, https://doi.org/10.1029/2000WR900207, 2000.

Bundesamt für Energiewirtschaft: Richtlinien zum Schutze des Bodens beim Bau unterirdisch verlegter Rohrleitungen, Schweiz, 1997.

Capparelli, G. and Spolverino, G.: An Empirical Approach for Modeling Hysteresis Behavior of Pyroclastic Soils, Hydrology, 7, 14, https://doi.org/10.3390/hydrology7010014, 2020.

Chen, S. and Guo, W.: Auto-Encoders in Deep Learning—A Review with New Perspectives, Mathematics, 11, 1777, https://doi.org/10.3390/math11081777, 2023.

D. N. Moriasi, J. G. Arnold, M. W. Van Liew, R. L. Bingner, R. D. Harmel, and T. L. Veith: Model Evaluation Guidelines for Systematic Quantification of Accuracy in Watershed Simulations, Trans ASABE, 50, 885–900, https://doi.org/10.13031/2013.23153, 2007.

den Ouden, H. E. M., Kok, P., and de Lange, F. P.: How Prediction Errors Shape Perception, Attention, and Motivation, Front Psychol, 3, https://doi.org/10.3389/fpsyg.2012.00548, 2012.

Fomin, D. S., Yudina, A. V., Romanenko, K. A., Abrosimov, K. N., Karsanina, M. V., and Gerke, K. M.: Soil pore structure dynamics under steady-state wetting-drying cycle, Geoderma, 432, 116401, https://doi.org/10.1016/j.geoderma.2023.116401, 2023.

Fu, Y. P., Liao, H. J., Chai, X. Q., Li, Y., and Lv, L. L.: A Hysteretic Model Considering Contact Angle Hysteresis for Fitting Soil-Water Characteristic Curves, Water Resour Res, 57, https://doi.org/10.1029/2019WR026889, 2021.

Gallipoli, D., Gens, A., Sharma, R., and Vaunat, J.: An elasto-plastic model for unsaturated soil incorporating the effects of suction and degree of saturation on mechanical behaviour, Géotechnique, 53, 123–135, https://doi.org/10.1680/geot.2003.53.1.123, 2003.

Gholamy, A., Kreinovich, V., and Kosheleva, O.: Why 70/30 or 80/20 Relation Between Training and Testing Sets: A Pedagogical Explanation, University of Texas at El Paso., 1–6 pp., 2018.

718   Gupta, H. V. and Kling, H.: On typical range, sensitivity, and normalization of Mean Squared Error and
719   Nash-Sutcliffe Efficiency type metrics, Water Resour Res, 47,
720   https://doi.org/10.1029/2011WR010962, 2011.

721   Gupta, H. V., Sorooshian, S., and Yapo, P. O.: Status of Automatic Calibration for Hydrologic Models:
722   Comparison with Multilevel Expert Calibration, J Hydrol Eng, 4, 135–143,
723   https://doi.org/10.1061/(ASCE)1084-0699(1999)4:2(135), 1999.

724   Gupta, S., Lehmann, P., Bickel, S., Bonetti, S., and Or, D.: Global Mapping of Potential and Climatic
725   Plant-Available Soil Water, J Adv Model Earth Syst, 15, https://doi.org/10.1029/2022MS003277,
726   2023.

727   Hannes, M., Wollschläger, U., Wöhling, T., and Vogel, H. -J.: Revisiting hydraulic hysteresis based on
728   long-term monitoring of hydraulic states in lysimeters, Water Resour Res, 52, 3847–3865,
729   https://doi.org/10.1002/2015WR018319, 2016.

730   Holthusen, D., Peth, S., and Horn, R.: Impact of potassium concentration and matric potential on soil
731   stability derived from rheological parameters, Soil Tillage Res, 111, 75–85,
732   https://doi.org/10.1016/j.still.2010.08.002, 2010.

733   IDAWEB: https://gate.meteoswiss.ch/idaweb/login.do, last access: 22 July 2024.

734   Ioffe, S., and Szegedy, C.: Batch normalization: Accelerating deep network training by reducing
735   internal covariate shift, arXiv [preprint], arXiv:1502.03167, 11 February 2015.

736   Jain, S. K., Singh, V. P., and van Genuchten, M. Th.: Analysis of Soil Water Retention Data Using
737   Artificial Neural Networks, J Hydrol Eng, 9, 415–420, https://doi.org/10.1061/(ASCE)1084-
738   0699(2004)9:5(415), 2004.

739   Kingma, D. P., and Ba, J.: Adam: A method for stochastic optimization, CoRR, arXiv:1412.6980, 22
740   December 2014.

741   Lu, L.: Dying ReLU and Initialization: Theory and Numerical Examples, Commun Comput Phys, 28,
742   1671–1706, https://doi.org/10.4208/cicp.OA-2020-0165, 2020.

743   Lu, N., Godt, J. W., and Wu, D. T.: A closed-form equation for effective stress in unsaturated soil,
744   Water Resour Res, 46, https://doi.org/10.1029/2009WR008646, 2010.

745   Ma, Y., Liu, H., Yu, Y., Guo, L., Zhao, W., and Yetemen, O.: Revisiting Soil Water Potential: Towards a
746   Better Understanding of Soil and Plant Interactions, Water (Basel), 14, 3721,
747   https://doi.org/10.3390/w14223721, 2022.

748   Mendes, J. and Buzzi, O.: New insight into cavitation mechanisms in high-capacity tensiometers
749   based on high-speed photography, Canadian Geotechnical Journal, 50, 550–556,
750   https://doi.org/10.1139/cgj-2012-0393, 2013.

751   Menon, M., Mawodza, T., Rabbani, A., Blaud, A., Lair, G. J., Babaei, M., Kercheva, M., Rousseva, S.,
752   and Banwart, S.: Pore system characteristics of soil aggregates and their relevance to aggregate
753   stability, Geoderma, 366, 114259, https://doi.org/10.1016/j.geoderma.2020.114259, 2020.

754   Montesinos López, O. A., Montesinos López, A., and Crossa, J.: Fundamentals of Artificial Neural
755   Networks and Deep Learning, in: Multivariate Statistical Machine Learning Methods for Genomic
756   Prediction, Springer International Publishing, Cham, 379–425, https://doi.org/10.1007/978-3-030-
757   89010-0_10, 2022.

758 Nash, J. E. and Sutcliffe, J. V.: River flow forecasting through conceptual models part I — A discussion
759 of principles, J Hydrol (Amst), 10, 282–290, https://doi.org/10.1016/0022-1694(70)90255-6, 1970.

760 Rawls, W. J., Pachepsky, Y. A., Ritchie, J. C., Sobecki, T. M., and Bloodworth, H.: Effect of soil organic
761 carbon on soil water retention, Geoderma, 116, 61–76, https://doi.org/10.1016/S0016-
762 7061(03)00094-6, 2003.

763 Reichle, R. H., Liu, Q., Koster, R. D., Crow, W. T., De Lannoy, G. J. M., Kimball, J. S., Ardizzone, J. V.,
764 Bosch, D., Colliander, A., Cosh, M., Kolassa, J., Mahanama, S. P., Prueger, J., Starks, P., and Walker, J.
765 P.: Version 4 of the SMAP Level-4 Soil Moisture Algorithm and Data Product, J Adv Model Earth Syst,
766 11, 3106–3130, https://doi.org/10.1029/2019MS001729, 2019.

767 Ritter, A. and Muñoz-Carpena, R.: Performance evaluation of hydrological models: Statistical
768 significance for reducing subjectivity in goodness-of-fit assessments, J Hydrol (Amst), 480, 33–45,
769 https://doi.org/10.1016/j.jhydrol.2012.12.004, 2013.

770 Romero-Ruiz, A., Linde, N., Keller, T., and Or, D.: A Review of Geophysical Methods for Soil Structure
771 Characterization, Reviews of Geophysics, 56, 672–697, https://doi.org/10.1029/2018RG000611,
772 2018.

773 Ross, P. J. and Smettem, K. R. J.: A Simple Treatment of Physical Nonequilibrium Water Flow in Soils,
774 Soil Science Society of America Journal, 64, 1926–1930,
775 https://doi.org/10.2136/sssaj2000.6461926x, 2000.

776 Rostami, A., Habibagahi, G., Ajdari, M., and Nikooee, E.: Pore Network Investigation on Hysteresis
777 Phenomena and Influence of Stress State on the SWRC, International Journal of Geomechanics, 15,
778 https://doi.org/10.1061/(ASCE)GM.1943-5622.0000315, 2015.

779 Sadeghi, H., Chiu, A. C. F., Ng, C. W. W., and Jafarzadeh, F.: A vacuum-refilled tensiometer for deep
780 monitoring of in-situ pore water pressure, Scientia Iranica, 27, 596–606,
781 https://doi.org/10.24200/sci.2018.5052.1063, 2018.

782 Shwetha, P. and Varija, K.: Soil Water Retention Curve from Saturated Hydraulic Conductivity for
783 Sandy Loam and Loamy Sand Textured Soils, Aquat Procedia, 4, 1142–1149,
784 https://doi.org/10.1016/j.aqpro.2015.02.145, 2015.

785 Smith, C. W., Johnston, M. A., and Lorentz, S. A.: The effect of soil compaction on the water
786 retention characteristics of soils in forest plantations, South African Journal of Plant and Soil, 18, 87–
787 97, https://doi.org/10.1080/02571862.2001.10634410, 2001.

788 Spreafi, M. and Weingartner, R.: The Hydrology of Switzerland Selected aspects and results, Reports
789 of the FOWG, Water Series, Bern, 2005.

790 Tuller, M. and Or, D.: Soil water retention and characteristic curve, in: Encyclopedia of Soils in the
791 Environment, Elsevier, 187–202, https://doi.org/10.1016/B978-0-12-822974-3.00105-1, 2023.

792 Willems, P.: A time series tool to support the multi-criteria performance evaluation of rainfall-runoff
793 models, Environmental Modelling & Software, 24, 311–321,
794 https://doi.org/10.1016/j.envsoft.2008.09.005, 2009.

795 Zuo, Y. and He, K.: Evaluation and Development of Pedo-Transfer Functions for Predicting Soil
796 Saturated Hydraulic Conductivity in the Alpine Frigid Hilly Region of Qinghai Province, Agronomy, 11,
797 1581, https://doi.org/10.3390/agronomy11081581, 2021.